Superfluid helium-3 in cylindrical restricted geometries : a study with low-frequency NMR

Benningshof, O.W.B.

Citation

Benningshof, O. W. B. (2011, March 30). *Superfluid helium-3 in cylindrical restricted geometries : a study with low-frequency NMR*. Retrieved from https://hdl.handle.net/1887/16677

Chapter 3

Spin waves in cylinder of 1 mm in diameter

3.1 Spin waves

Spin waves refer to a collective excitation of spins in a system, for example electron spins in a lattice. In analogy with lattice vibrations or phonons, which are collective excitations of atomic positions in a lattice. Quantum mechanically one can speak about magnons, which are then the quantized spin waves. In the case of ^{3}He, NMR is the ideal technique to detect such spin waves, but the measured signal is the integrated magnetization of the spins of ^{3}He, which will average to zero [1]. However, standing spin waves will give a detectable signal. One way to create standing spin waves is to apply an inhomogeneous magnetic field, which allows even the detection of spin waves in the normal phase of ^{3}He [56]. In the superfluid phases the inhomogeneity of the texture allows the existence of standing waves as well. Here the spin waves are the Goldstone modes associated with the spontaneously broken rotational symmetry in spin space [2].

The bulk isotropic superfluid B-phase of ^{3}He is not suitable to form standing spin waves measurable with conventional NMR techniques, since the $\hat{\mathbf{n}}$-vector has no preferred orientation, causing the integrated magnetization to average to zero. However, walls and magnetic fields will introduce a preferred orientation for the $\hat{\mathbf{n}}$-vector, which is explained in detail in section 3.3.

In confined geometries including magnetic fields the orientation of the $\hat{\mathbf{n}}$-vector will be locally different, which results in the bending of the $\hat{\mathbf{n}}$-vector over the sample. This bending occurs over a typical distance of the magnetic healing length ξ_H, which is

---

[1] Technically one can measure a net magnetization if the NMR coils are of the same dimension as the wavelength of the system, which is normally not the case.

[2] In the case of ^{3}He-B the relative broken spin-orbit symmetry.

a few millimeters long [57] [58]. If the superfluid B-phase is formed in such geometry, with at least one dimension close to the magnetic healing length, it will create a texture which may act as a potential for standing spin waves. These spin waves can be detected by transverse NMR experiments, and are observed as satellite peaks in the absorption spectrum.

The very first experiment which observed spin waves in the superfluid B-phase was performed by Osherhoff, see for example [59]. He used a slab geometry (separations of the plates was $L \leq \xi_H$) and a magnetic field $\mathbf{B}_0$ parallel to the plates. The transverse NMR experiment found a more or less constant separation of the spin wave modes (NMR resonances), of which the intensities dropped as function of k^{-1} (k is the spin wave mode). This was in good agreement (at least to first order) with the solutions of the differential equation for this geometry [60] [61], see also section 3.5. It was seen as the proof of the existence and possibility of spin waves in the superfluid B-phase.

Another convenient geometry to create spin waves is a cylinder with a radius of few times the magnetic healing length. The cylindrical symmetry makes it relatively easy to calculate the allowed textures and spin waves, see sections 3.4 and 3.5. One of the first transverse spin wave experiments in a cylindrical geometry was performed by Hakonen *et al.* [62]. The experiment also showed a nearly equal separation between the spin wave modes, of which the intensity decreased as a function of k. These experiments could be explained by numerical calculations of Jacobsen and Smith [63].

The cylindrical geometries were also convenient to study vortices in the superfluid B-phase. Consequently several groups build rotating nuclear refrigerators to study this phenomena [64] [65] [66] [67] [68] [69]. Vortices affect the $\hat{\mathbf{n}}$-vector mainly through a change in the magnetic orientation energy, which results in a different textural configuration compared to the non-rotational situation [70]. The effects show up in the experiments by a change of intensity and spacing of the spin waves. In this way an interesting discontinuity in the spin wave resonant frequencies was observed [58] [62], which marks a transition between the two different vortex states in the B-phase.

Our interest concerns the non-rotating cylinder experiment. We are interested in the textural configuration in the cylinder, which should be revealed by the spin waves. The magnetic healing length decreases as a function of temperature, and with a sufficiently small container radius one expects a textural transition. However, we found that the $\hat{\mathbf{n}}$-texture formed a metastable configuration, which is unchanged to the lowest temperature. Not only did this metastable texture create a temperature independent potential for the spin waves, but the form of the potential is close to a quadratic function. This makes the potential interesting for two reasons. First, it is pressure and temperature independent, which is different from the situation in earlier spin wave experiments. However, modifying the pressure will still change the dipole coherence length of the superfluid, which will increase (or decrease) the amount of spin wave modes in the container. Meaning that we can now study this effect in the same energy 'landscape'. Secondly, the differential equation describing this geometry is analytically solvable for a quadratic potential, and allows us to explain the absorption intensities of the spin wave modes. This is a unique phenomenon in the superfluid B-phase spin wave experiments.

The theory and the experiments of the spin waves in the metastable texture are described in this chapter. Also the experiments with the textural transition to the expected uniform texture is included in this chapter. From that experiment we conclude that the metastable texture could be realize if its growing speed is sufficiently slow.

3.2 Transverse NMR in ^{3}He-B

Normally, in the absence of magnetic field, the spin orientation in a sample is isotropic. In that case, when cw-NMR is applied, there is resonance at the Larmor frequency as described in section 2.4. However, the order parameter of ^{3}He can be anisotropic (including the spin orientation), which induces a shift in the resonance frequency compared to the Larmor frequency. In cw-NMR experiments a shift in the resonance frequency will occur when a transverse oscillation $\Omega_\perp$ of the spins contributes to the (transverse) oscillation of the rf-field from $\mathbf{B}_1$. The new transverse resonant frequency ω_0 will then be

$$\omega_0{}^2 = \omega_L{}^2 + \Omega_\perp{}^2. \tag{3.1}$$

As already mentioned before, the dipole energy (despite the fact that it is small by itself) has strong influence on the orientation of the order parameter, and thus on the frequency shift. From the Hamiltonian describing the spin orientation of the system,

$$H_S = \frac{1}{2}\gamma^2 \mathbf{S}\boldsymbol{\chi}^{-1}\mathbf{S} - \gamma \mathbf{S}\cdot\mathbf{H} + H_D, \tag{3.2}$$

where $\boldsymbol{\chi}$ is the susceptibility tensor, the spin dynamics in the superfluid can be derived [21], [71], [72]. From here the oscillator frequencies can be obtained. In the linear regime, meaning small deviations from the equilibrium values (spatially homogenous conditions), the oscillator frequencies get the form of

$$\Omega^2_{\mu\nu} = \frac{\gamma^2}{\chi}\frac{\partial^2 f_D}{\partial\theta_\mu \partial\theta_\nu}. \tag{3.3}$$

If one would apply the dipole energy of the (zero field) B-phase (1.23) to this equation one would not expect a transverse component, since the orientation of the $\hat{\mathbf{n}}$-vector is isotropic. However, if we take the limit for the magnetic field $H \to 0$, keeping $\hat{\mathbf{n}}$ parallel to the magnetic field $\mathbf{H}$, equation (1.23) changes into

$$F_D^B = \frac{8}{5} g_D(T)\left(\cos\theta_z + \frac{1}{4}\right)^2 + const. \tag{3.4}$$

From equation (3.3) and by putting $\theta_z = \theta_L$ we get:

$$\Omega_{xx} = \Omega_{yy} = 0, \tag{3.5}$$

$$\Omega^2_{zz} = 3\frac{\gamma^2}{\chi_B} g_D(T) \equiv \Omega^2_B. \tag{3.6}$$

As expected, the B-phase does not have transverse frequency components, but it has a longitudinal one. This would not be observed in a transverse cw-NMR experiment, but can be seen in longitudinal cw-NMR experiment, hence with the rf-field $\mathbf{B}_1$ parallel with $\mathbf{B}_0$. These longitudinal resonances have been observed experimentally [73], [36].

In the B$_2$-phase one would expect, due to preferred orientation of the $\hat{\mathbf{n}}$-vector, a transverse frequency shift from the Larmor frequency. Using the relations (1.24) and (1.28) with (3.3) and including only small deviations around equilibrium, one obtains the transverse components [21]

$$\Omega_{xx}^2 = \Omega_{yy}^2 = \frac{2}{5}\lambda_D N_F \gamma^2 \chi^{-1}(\Delta_\perp^2 - \Delta_\parallel^2). \tag{3.7}$$

It implies two elliptical polarization modes with frequencies:

$$\omega^2 = \frac{1}{2}\omega_L^2 + \Omega_{xx} \pm \frac{1}{2}\omega_L\sqrt{(\omega_L^2 + 4\Omega_{xx}^2)}. \tag{3.8}$$

Because we do low-frequency NMR in our experiments the difference in population $(\Delta_\perp^2 - \Delta_\parallel^2)$ is rather small. The transfer shift due to the orientation effects in the B$_2$-phase can be neglected, especially because there is a much more dominating effect on the transverse shift.

If one studies NMR in restricted geometries like cylinders, slabs, aerogel or powders, surface effects play a dominating role on the orientation of the order parameter $\hat{\mathbf{n}}$, see section 3.3. The $\hat{\mathbf{n}}$-vector will orientate from equilibrium $\hat{\mathbf{n}} \parallel \mathbf{H}$ to the normal of the surface. This transverse shift ω_0 can be expressed in the longitudinal resonance frequency of the B-phase (see equation (3.6)) and the angle β, which is the angle between the $\hat{\mathbf{n}}$-vector and the (external) applied magnetic field [74]:

$$\omega_0^2 = \frac{1}{2}(w_L^2 + \Omega_B^2) + \sqrt{\frac{1}{4}(\omega_L^2 + \Omega_B^2)^2 - \omega_L^2\Omega_B^2\cos^2\beta}. \tag{3.9}$$

The angle β is a function of position in the cell, so the total NMR spectrum from the ^{3}He fluid, if we neglect field inhomogeneity and relaxation times, is then given by the line shape function

$$f(\omega) = \int_V d^3\mathbf{r}\,\delta[\omega - \omega_0(\mathbf{r})]. \tag{3.10}$$

3.3 Orientation of the $\hat{\mathbf{n}}$-vector due to bulk and surface effects

The orientation of the $\hat{\mathbf{n}}$-vector is determined by effects in the bulk liquid and by the surface of the sample. The two most important orientation energies in the bulk are: The bulk-field free energy F_{BH} and the bulk-bending free energy F_{BB}.

The bulk-field free energy F_{BH} equals the $\hat{\mathbf{n}} \cdot \mathbf{H}$ dependency of the dipole energy density (1.24) to lowest order. Higher orders are not needed, because they hardly give any contribution to the bulk-field free energy.

$$F_{BH} = -a \int d^3r (\hat{\mathbf{n}} \cdot \mathbf{H})^2. \tag{3.11}$$

The term $(\hat{\mathbf{n}} \cdot \mathbf{H})^2$ is described by Leggett [21] as a combination of the depairing effects of the magnetic field and the dipole energy. The coupling strength a, in the case of ^{3}He-B, is estimated to be $|a| \sim 4 \cdot 10^{-12}$ erg cm^{-3} G^{-2} [55] , [22], [75]. The magnetic field in the bulk will try to orientate $\hat{\mathbf{n}}$ in the same direction, for which the energy is minimized.

The $\hat{\mathbf{n}}$-vector is oriented by local conditions, however the change of this orientation can only be continuous. Fast changes (discontinuities) of the order parameter will be energetically unfavorable. It means that all spatial variations should be smoothed (out) over a finite distance, which is accomplished if F_{BB} is expressed as an invariant combination of the gradients of the order parameter [76], [60]. Basically, the bulk-bending free energy is obtained by integrating the bending free energy density (1.35) over the whole volume.

$$\begin{aligned} F_{BB} = \frac{c}{13} \int d^3r \{ & 16(\hat{\mathbf{n}} \times (\nabla \times \hat{\mathbf{n}}))^2 + 13(\nabla \cdot \hat{\mathbf{n}})^2 + 11(\hat{\mathbf{n}} \cdot \nabla \times \hat{\mathbf{n}})^2 \\ & - 2\sqrt{15}(\nabla \cdot \hat{\mathbf{n}})(\hat{\mathbf{n}} \cdot \nabla \times \hat{\mathbf{n}}) + 16\nabla \cdot [(\hat{\mathbf{n}} \cdot \nabla)\hat{\mathbf{n}} - \hat{\mathbf{n}}(\nabla \cdot \hat{\mathbf{n}})]\}, \end{aligned} \tag{3.12}$$

where $|c| \sim 4 \cdot 10^{-10}(\rho_s/\rho)$ erg cm^{-1}, and (ρ_s/ρ) the fraction between the superfluid and the normal liquid in a static configuration [55], [22], [75].

The most important energies, responsible for the orientation of the $\hat{\mathbf{n}}$-vector at the wall, are the surface-dipole free energy F_{SD} and the surface-field free energy F_{SH}. The surface-dipole free energy F_{SD} deals with the fact that the orbital angular momentum $\mathbf{L}$ of the Cooper pairs at the wall are suppressed as:

$$F_{SD} = -b \int d^2r (\hat{\mathbf{n}} \cdot \hat{\mathbf{s}})^2, \tag{3.13}$$

where $|b| \sim 1 \cdot 10^{-10} \Delta(T)/\Delta(0)$ erg cm^{-2} and $\Delta(T)/\Delta(0)$ indicates the amount of Cooper pairs [55] , [22], [75]. $\hat{\mathbf{s}}$ is the surface normal, and parallel alignment of $\hat{\mathbf{n}}$ will minimize the total energy.

When a magnetic field is included, there is a competition between the surface and field aligning forces. The energies of this interplay are expressed in the surface-field free energy F_{SH} [60] :

$$\begin{aligned} F_{SH} &= -d \int d^2 r (\hat{\mathbf{s}} \cdot \mathbf{R} \cdot \mathbf{H})^2 \\ &= -\frac{25}{16} d \int d^2 r [(\hat{\mathbf{n}} \cdot \hat{\mathbf{s}})(\hat{\mathbf{n}} \cdot \mathbf{H}) + \sqrt{\frac{3}{5}} \hat{\mathbf{n}} \cdot (\hat{\mathbf{s}} \times \mathbf{H}) - \frac{1}{5} (\hat{\mathbf{s}} \cdot \mathbf{H})]^2, \end{aligned} \tag{3.14}$$

where $\mathbf{R}$ is the rotation matrix specified by $\hat{\mathbf{n}}(\mathbf{r})$ and θ (1.16). The second part of the equation is obtained by insertion the rotation matrix with the angle $\theta = \theta_L = \cos^{-1}(-\frac{1}{4})$ (for which the dipole energy is minimized in the bulk liquid). The coefficient d is approximately $\xi(T)(\chi_N - \chi_B)$. The difference in susceptibility $(\chi_N - \chi_B)$ between the normal- and the B-phase (Balian-Werthamer state) is maximum at zero temperature, which is approximately $2/3\chi_N$. The temperature dependent coherence length $\xi(T)$ comes in as a length scale over which the order parameter can recover.

The preferred orientation of $\hat{\mathbf{n}}$, for which F_{SH} is minimized, also depends on the relative direction of $\mathbf{H}$ and $\hat{\mathbf{s}}$. In the case that $\mathbf{H}$ is perpendicular to $\hat{\mathbf{s}}$, as in the case of our experiments, it is shown [60] that F_{SH} is minimized when $\hat{\mathbf{n}}$ makes an angle $\beta = \cos^{-1}(1/\sqrt{5}) \simeq 63.4°$ with respect to both $\hat{\mathbf{s}}$ and $\mathbf{H}$. This situation is illustrated in the figure 3.1, taken from the article by Spencer and Ihas [77].

All these forces mentioned above (and other higher order forces) do want to align the $\hat{\mathbf{n}}$-vector in the most (energetically) favorable orientation corresponding to that force. However, the superfluid takes the configuration which minimizes the total free energy over the whole sample. This results in continues change of the orientation from the $\hat{\mathbf{n}}$-vector over the whole sample, which is called the $\hat{\mathbf{n}}$-texture [76].

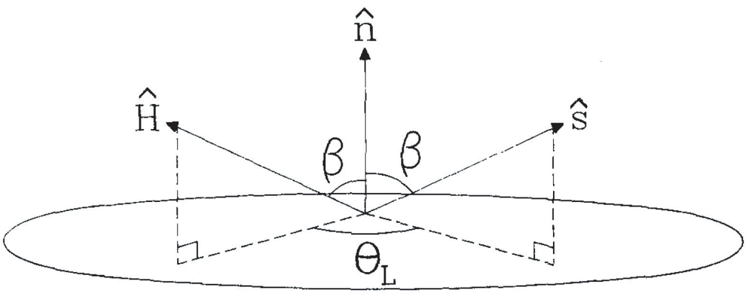

Figure 3.1: The vectors $\mathbf{H}$, $\hat{\mathbf{s}}$, and $\hat{\mathbf{n}}$ shown relative to a plane perpendicular to $\hat{\mathbf{n}}$ when the surface normal $\hat{\mathbf{s}}$ and magnetic field $\mathbf{H}$ are perpendicular. The angles are given by $\hat{\mathbf{n}} \cdot \hat{\mathbf{s}} = \hat{\mathbf{n}} \cdot \mathbf{H}/H = \cos\beta = 1/\sqrt{5}$ and $\cos\theta_L = -1/4$. Rotation by θ_L about the axis $\hat{\mathbf{n}}$ takes the $\hat{\mathbf{s}}$ vector into the $\mathbf{H}$ vector.

From the four coefficients of the equations (3.11), (3.12), (3.13) and (3.14) we can define one important characteristic length R_c and two characteristic fields H_S and H_B.

$$R_c = \frac{c}{b}. \tag{3.15}$$

This length defines the typical sample size for which the surface-determined orientation of the $\hat{\mathbf{n}}$-vector is noticeable in the bulk liquid of the sample. When the size of the sample is much bigger than this length, the surface energy becomes more important than the bending energy.

The definition of the characteristic field H_S is given by

$$H_S = \sqrt{\frac{b}{d}}. \tag{3.16}$$

This parameter indicates which surface energy, namely the surface-dipole or the surface-field free energy, is dominating. In low fields the surface-dipole free energy determines the orientation of the $\hat{\mathbf{n}}$-vector and in high fields the surface-field free energy will.

Finally, the characteristic field

$$H_B = \frac{b^2}{ac}. \tag{3.17}$$

This field indicates whether the bulk or the surface effects have most influence on the orientation on the $\hat{\mathbf{n}}$-vector.

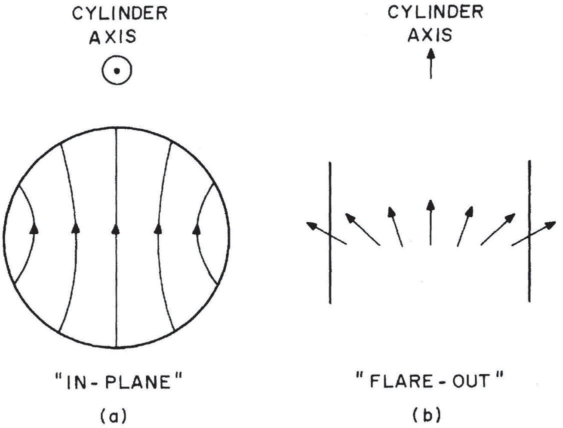

Figure 3.2: Orientation of the $\hat{\mathbf{n}}$-vector in cylindrical symmetry. (a) in-plane texture and (b) the flare-out texture. Orientation of the cylinder is indicated.

3.4 Orientation of the $\hat{\mathbf{n}}$-vector in cylindrical samples

In general different textures (in different geometrically samples) seem to be possible. Even in a cylindrical sample, many stable textures can be expected. However, in the case of an axial magnetic field two stable textures are calculated by Smith, Brinkman and Engelsberg [60]. In the absence of a magnetic field (or the limit to zero), the $\hat{\mathbf{n}}$-vector's orientation is determined by a competition of the bulk-bending free energy and the surface-dipole free energy. If the radius R of the cylinder is close to the characteristic length R_c, the in-plane texture is energetically favorable. Here the $\hat{\mathbf{n}}$-vector has no component along the z-axis, see figure 3.2 (a) (figure is taken from the article of Smith, Brinkman and Engelsberg [60]). The bulk-bending free energy determines this texture as long as the radius of the cylinder is $R < 10.0R_c$. However for very small R there are some deviations to this texture, due to boundary conditions at the surface.

If the radius of the cylinder is $R \gg R_c$, than the surface energy gets more important [3]. In this case the boundary conditions put $\hat{\mathbf{n}} \parallel \hat{\mathbf{s}}$, with $\hat{\mathbf{s}}$ the normal to the cylinder wall. As this is impossible in an in-plane texture, the consequence is that the $\hat{\mathbf{n}}$-vector has to flare out into the z-direction of the cylinder, see figure 3.2 (b). In the absence of a magnetic field the flare-out configuration is the lowest energy configuration as long as $R \geq 10.0R_c$. While it is intuitively clear that axial magnetic fields will favor the flare-out texture, it is generally hard to calculate the reduction of R, for which the crossover between the two textures occurs. However, perturbation theory is done

---

[3] The bulk-bending free energy increases like $\ln(R/R_c)$.

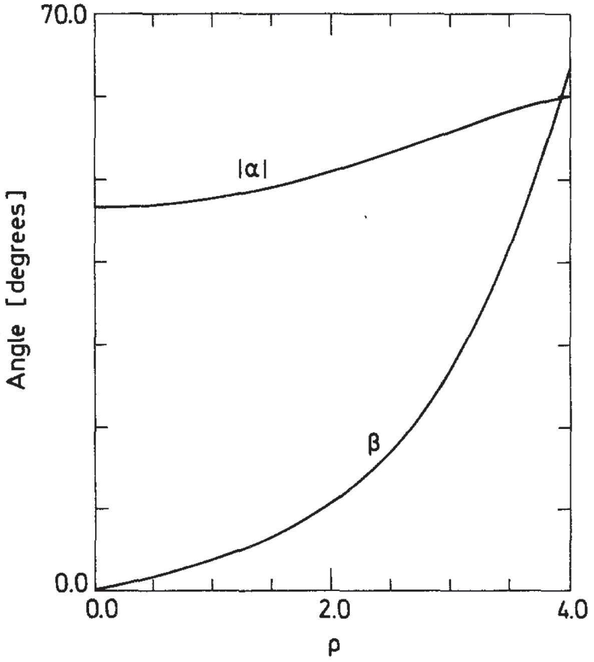

Figure 3.3: The radial dependence of the azimuthal angle α and the polar angle β for a cylinder of radius R. $\rho \equiv r/\tilde{\xi}_H$. The radius $R = 4\tilde{\xi}_H = 4\sqrt{65/8}\xi_H$.

[60], and for small field ($H \ll H_S \wedge H \ll H_B$) the crossover is at a radius of:

$$R = 10.0R_c - 137(H/H_B)^2 R_c. \tag{3.18}$$

For higher magnetic fields ($H \gg H_S$) the surface-field free energy is smaller than the surface-dipole free energy. Here we expect that the $\hat{\mathbf{n}}$-vector is parallel to the z-axis in the center of the cylinder and aligns itself over a typical length ξ_H (magnetic healing length) to the orientation directed by the surface-field free energy ($\hat{\mathbf{n}}$ has an angle with $\mathbf{H}$ and $\hat{\mathbf{s}}$ of $\cos^{-1}(1/\sqrt{5})$). These two boundary conditions change the $\hat{\mathbf{n}}$-vector orientation in a spiral-like configuration, which may be parameterized by

$$\hat{\mathbf{n}} = \sin\beta\cos\alpha\hat{\mathbf{r}} + \sin\beta\sin\alpha\hat{\varphi} + \cos\beta\hat{\mathbf{z}} \tag{3.19}$$

in cylindrical coordinates. The angles α and β are functions of r only. Its behavior has been studied analytically [78], [79] and numerically [63]. The dependence of α and β do matter on the cylinder size as well, it changes the boundary conditions for α (it may vary between 60° to 38° for $\alpha(0)$) and the way β varies over the sample.

At this point it is convenient to express the radius of the cylinder in terms of ξ_H, the magnetic healing length of ^{3}He-B. We know as long as there is sufficient magnetic

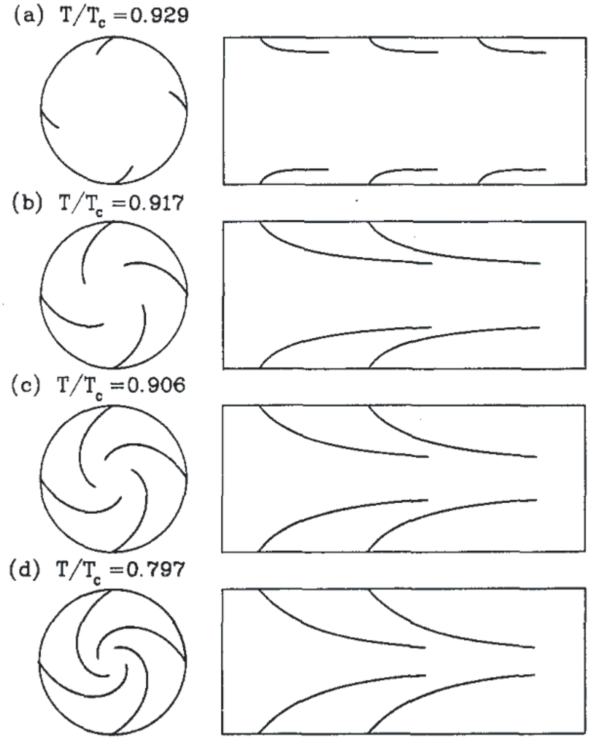

Figure 3.4: Some views of the growing $\hat{\mathbf{n}}$-texture obtained from the experiment of Spencer and Ihas. Figure is taken from [57].

field the flare-out configuration is favorable. In other words, as long as the radius is at least a couple of times ξ_H the texture should be in the flare-out configuration. So, in the case we deal with cylinders where $R > \xi_H$, the boundary conditions for β are: $\beta(R) = \cos^{-1}(1/\sqrt{5}) \approx 63.4°$ and $\beta(0) = 0$. The angle β changes quadratically for small r with some exponential prefactor. On the other hand, α hardly changes as function of r and is plotted together with β, in the case $R = 4\tilde{\xi}_H = 4\sqrt{65/8}\xi_H$, in figure 3.3. This figure is taken from the article of Jacobsen and Smith [63]. Here the two angles α and β are connected such that the total free energy was minimized.

Experimentally the r-dependence of the two angles was already found by Spencer and Ihas in 1982 [57], and was later worked out in detail [77]. In their transverse NMR experiments they could find the $\beta(r)$ and $\alpha(r)$ by deconvoluting their NMR spectra. As explained in equation (1.39) the magnetic healing length ξ_H grows with decreasing temperature, which enabled them to model the texture growing as it is parameterized by (3.19), see figure 3.4. It is interesting to see, and important for us as we will see later, that the texture gradually grows in a spiral way to the center. The growing

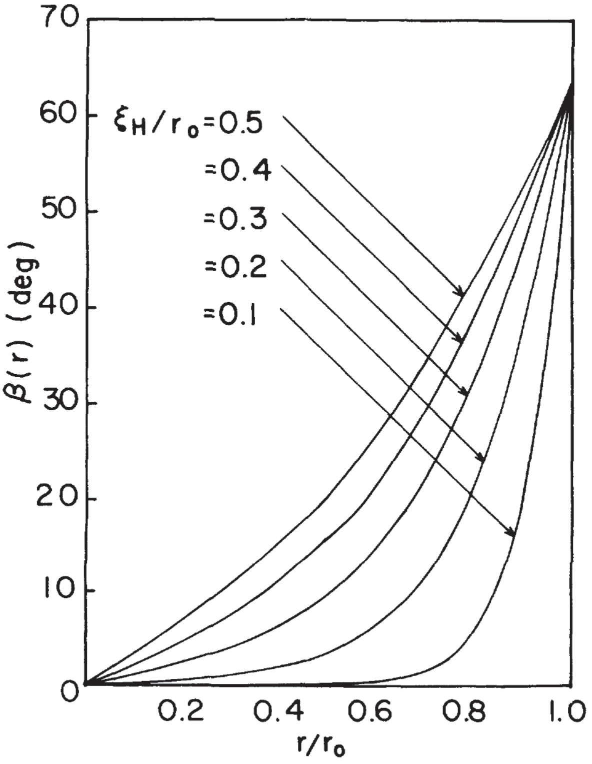

Figure 3.5: $\beta(r)$ for several values of ξ_H/r_0. Figure taken from [79].

should be able to continue as long as the boundary conditions can be fulfilled, meaning that the flare-out texture will grow as long it is the most energetically favorable configuration.

As mentioned before, much effort is done to calculate the radial behavior of β. The results of Maki and Nakahara [79], who calculated β for different ratios of ξ_H/r_0 are plotted in figure 3.5. All these simulations support the flare-out configuration. Simulations for ratios $\xi_H/r_0 > 0.5$ become hard, as it cannot be approximate linearly. However, one may assume that the most extreme form of the flare-out configuration would be a straight line connecting the boundary conditions, which corresponds to a gradual change of the $\hat{\mathbf{n}}$-vector over the sample. Not clear is how this is energetically in proportion to other textures. Actually, because of complications in the calculations, it is not clear at all how transitions to other textures should occur when $\xi_H \geq R$. Of course the qualitative answer for the limit $\xi_H \gg R$ is clear. The texture should be completely uniform, and β should have an angle of $\cos^{-1}(1/\sqrt{5})$, as is imposed by the surface.

3.5 Spin dynamics in a non-uniform texture

The influence of non-uniform textures on spin dynamics can be solved with the Hamiltonian approach. In this case the Hamiltonian of equation (3.2) should be extended with the gradient free energy density of equation (1.31). By assuming the following: The equilibrium $\hat{\mathbf{n}}$ varies on a scale of ξ_H, θ_μ varies on a scale of ξ_D (which is much longer than ξ_H, see section (1.8)), spin-orbit angle is fixed ($\theta = \theta_L$) and parameterize the order parameter in terms of θ_μ, the bending energy is given as [60] [80]

$$f_{bend} = \frac{1}{2}\frac{\chi}{\gamma^2}\Omega_B^2\xi_D^2 \left\{ \bar{K}\sum_{\mu\nu}(\nabla_\mu\theta_\nu)^2 - \bar{K}'\left[\sum_{\mu\nu} R^L_{\mu\nu}(\nabla_\mu\theta_\nu)\right]^2 \right\}. \tag{3.20}$$

The coefficients are given by $\bar{K}' = \bar{K}_2 + \bar{K}_3$ and $\bar{K} = 2\bar{K}_1 + \bar{K}'$ with $\bar{K}_j = K_j\Delta^2\gamma^2/(\chi\Omega_B^2\xi_D^2)$. $R^L_{\mu\nu}$ is the rotation matrix at the dipole-locked rotation angle ($\theta = \theta_L$), which contains the information of the equilibrium $\hat{\mathbf{n}}$-vector (see equation (1.16)).

The spin equations (dynamics) can now be solved from the effective Hamiltonian, hence

$$i\hbar\dot{\mathbf{S}} = [\mathbf{S}, H_S + f_{bend}]. \tag{3.21}$$

Considering a weak rf-field $\mathbf{B}_1$ in a static uniform magnetic field $\mathbf{B}_0$ (determining the z-axis), Theodorakis and Fetter [81] showed that the following differential equation is obtained

$$(D_m + V_m)\theta_m = \frac{1}{\Omega_B^2}[(\omega^2 - m\omega\omega_L - \Omega_B^2)\theta_m - i\omega\gamma H_{1m}], \tag{3.22}$$

where $V_m = -1 + |\hat{\mathbf{n}_m}|^2$ and $D_m \equiv D_{mm}$:

$$D_{\mu\nu} = \xi_D^2\left[-\delta_{\mu\nu}\bar{K}\nabla^2 + \bar{K}'\sum_{\lambda\lambda'}(R^L_{\mu\lambda}\nabla_\lambda)(R^L_{\nu\lambda'}\nabla_{\lambda'})\right]. \tag{3.23}$$

The differential equation can be rewritten in the form of the Schrödinger equation (assuming that there is a no spin super current through the surface)

$$(D_m + V_m)\psi_{m,k} = E_{m,k}\psi_{m,k}. \tag{3.24}$$

Here D_m and V_m play the role of the kinetic and the potential energy, respectively. The polarization of the vector field is indicated with m. Transverse components coincide with + and - , and the longitudinal component with $m = 0$. The two equations can be connected by expressing θ in terms of eigenfunctions $\psi_{m,k}$:

$$\theta_m(\mathbf{r}) = \sum_k c_{m,k}\psi_{m,k} \tag{3.25}$$

where $c_{m,k}$ is chosen such that equation (3.22) can be regained. The relations of the (kth) eigenfrequencies and energies are then given by.

$$\omega_{m,k}^2 - m\omega_{m,k}\omega_L - \Omega_B^2 = E_{m,k}\Omega_B^2. \tag{3.26}$$

It is this set of frequencies, which correspond to spin waves, which can be experimentally accessed.

3.5.1 Cylindrical geometry

Spin waves can be expected if one goes to restricted geometries, where the surface plays an important role in the orientation of the $\hat{\mathbf{n}}$-vector. In general the differential equation (3.24) for a given geometry is not trivial to solve. However, for the parallel-plate and cylindrical geometries the differential equation, to a certain extent, can be solved. In the case of slab geometry (separation of the plates $L \leq \xi_H$) and $\mathbf{B}_0$ parallel to the plates, transverse NMR experiments could detect spin waves [59]. Here the spacing between the spin waves (NMR resonances) was (more or less) constant, and the intensity dropped as a function of k^{-1}. This is in good agreement (at least to first order) with the solution of the differential equation (3.24) for this geometry [82].

Our experiments are performed in a cylindrical geometry in a transverse NMR configuration. The effective potential V_m, see equation (3.22), for the transverse case ($m = +$), where the equilibrium $\hat{\mathbf{n}}$-vector for long circular cylinders is parameterized as in equation (3.19), is axially symmetric and given as:

$$V_+ = -1 + \frac{1}{2}\sin^2\beta. \tag{3.27}$$

In this axially symmetrical case the differential equation (3.24) is given by [79]:

$$(-\bar{K} + \bar{K}'|R_{+r}^L|^2)\xi_D^2 \left[\frac{1}{r}\frac{d}{dr}\left(r\frac{d}{dr}\right)\right]\psi_{+,k} - (1 - \frac{1}{2}\sin^2\beta)\psi_{+,k} = E_{+,k}\psi_{+,k} \tag{3.28}$$

If we are in the experimental situation, illustrated in figure (3.3), the potential V_+ varies (determined by its boundary condition) between -1 ($r = 0$) and $-3/5$ ($r = R$). It has a quadratic behavior near its center, and one may want to replace the $1/2\sin^2\beta$ part with $(r/L_1)^2$, where L_1 is a measure for the curvature bounded by the boundary conditions. By taking $|R_{+r}^L|^2 = 1/2$ (which is its value at r = 0), the differential equation reduces to the Schrödinger equation for the two dimensional harmonic oscillator. One may consider these approximation a bit rough (errors over 10% far from the center can be expected). However, it is, as shown later in this thesis, interesting to investigate which features a quadratic potential would show in the transverse NMR experiments.

The eigenvalues of the two dimensional harmonic oscillator are given by

$$E_{+,k} = -1 + 2\sqrt{\left(\bar{K} - \frac{1}{2}\bar{K}'\right)}\frac{\xi_D}{L_1}(k+1). \tag{3.29}$$

Only the s-wave states couple to the homogeneous rf-field, or with other words: only the $l = 0$ modes have non-vanishing intensities in experiments using uniform rf-fields [63]. Consequently, only the even k modes couple to the corresponding NMR frequencies. It means for the eigenvalues that they are equally spaced, like in the case of slab geometry. However, the relative intensity is given by:

$$I_k/I_0 = 1 \quad \text{for} \quad k = 2, 4, 6, ... \tag{3.30}$$

Where I_k is the intensity of the k^{th} spin wave mode. The NMR absorption lines for the excited modes should all show the same intensity. This is in sharp contrast with the planar $\hat{\mathbf{n}}$-textures, here the intensity drops as k^{-1}. However, experiments performed with cylindrical geometries do show a decrease of intensity with increasing k [62]. Jacobsen and Smith [63] did numerical calculations, where the configuration of the texture (which determines the effective potential) was determined by minimizing the appropriate free energy and solving the resulting Euler-Lagrange equations. It explained the experimental data, for which the quadratic potential approximation seemed to be too crude.

3.6 The magnetic healing length of ^{3}He-B

In section 1.8 a rough estimation of the magnetic healing length in the B-phase was performed. It shows the physical properties but it fails to describe the healing length in detail. The experimentally found magnetic healing length as function of temperature near melting curve pressures $\simeq$ 30 bar and 30 mT, as fitted by Maki and Nakahar [79], are put in figure 3.6. The fit was obtained from data at temperatures between the transition temperature T_c and 0.7 T_c. At lower temperatures an extrapolation of these fit functions was used. However, for the lowest temperatures it will more likely be proportional with the gap energy. Both fits show the same behavior before extrapolation and are approximately 0.5 mm for temperatures at 0.7 T_c and magnetic fields of 30 mT. In our experiments the magnetic field was half this value (15 mT), and according to (1.39) one should than expect a healing length of 1.0 mm. In addition equation (1.39) shows a ξ_0 dependence, which is 5 times longer for zero pressure compared to the melting pressures. It is reasonable to believe that our magnetic healing length is at least 5 mm for zero pressure, and $\sim$ 2.5 mm for 6 bar at 0.7 T_c and 15 mT [4].

3.7 NMR absorption in cylinder of 1 mm diameter

The NMR experiments performed in the cylindrical part of the cell with a cross section of 1 mm in diameter are done at relatively low pressures. Several measurements were done with a pressurized cell between 0 and 6 bar. The data is obtained by

---

[4] The data of Spencer and Ihas indeed show (roughly) 3 times longer magnetic healing length ξ_H^B for the low pressure data (2.89 bar) compared to the melting curve pressure.

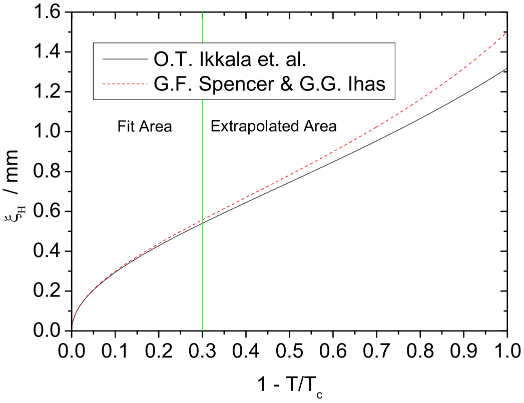

Figure 3.6: Fit of the magnetic healing length as function of temperature, obtained from the data from Spencer and Ihas [57] and Ikkala *et al.* [58]. Both have comparable systems with pressures around ~ 30 bar with magnetic fields of ~ 30 mT. The fit is obtained from data between T_c and 0.7 T_c. The curves at lower temperatures are extrapolates of the fit functions. Both areas are separated by the green line in the figure.

increasing temperature sweep, which gives 'better' thermal equilibrium and minimizes the hysteresis effects of the superfluid.

These measurements were all done in the same way. First the cell was put at the desirable pressure, same temperature far above the T_c of the superfluid. Then the whole system was cooled down by adiabatic cooling of the nuclear stage. Typically till temperatures of 0.3 T_c. At this point we waited till the whole system was in thermal equilibrium, as observed from the melting curve thermometer and the tuning fork. To increase the temperature, the magnetic field of the nuclear stage was slowly increased. Simultaneously, the cw-NMR measurements were started, and the data were collected nonstop by a labview controlled system.

The benefit to warming up the system adiabatically is that, at least ideally, the total amount of entropy is conserved. Measurements could be repeated much faster, without the time consuming pre-cooling of the nuclear stage. The disadvantage of this method is that stray fields of the magnet are not constant. While compensation coils reduce almost all the field at the experimental space, still a small fraction (around 0.01 %) can be seen in the NMR spectrum as a contribution to $\mathbf{B}_0$. Practically it is not a problem to compensate for this effect, especially considering the benefits of this method.

Increasing (slowly) the field constantly in time, results in a proportional increase of the temperature [5].

$$T = T^* + \frac{T^*}{B^*}\Delta B(t), \tag{3.31}$$

where T^* and B^* are the initial temperature and magnetic field and $\Delta B(t)$ the field added at B^* after $t = 0$. Typically the temperature was increased by 0.31 mK h^{-1}. The sweep time for the cw-NMR was typically 7 minutes, which means that the temperature increases by ~ 35 μK from start to end. Significant changes in the NMR spectra happen at much longer temperature scales. Meaning that temperature sweep is sufficient to map a good temperature dependence with the NMR technique.

A typical temperature sweep of the NMR spectrum is plotted in figure 3.7. Here the measurement is performed at 6 bar, and the temperature is swept between 0.57 mK and 1.56 mK (transition temperature).

At and above T_c the resonance frequency occurs at the Larmor frequency. Below T_c and at this pressure, the ^{3}He will have a transition from the normal phase to the B-phase. Technically, due to the magnetic field of NMR, it is in the B_2-phase. However, the NMR frequencies are low, meaning the population differences are approximately zero, see equation (1.30). To a very good approximation the values of the spin susceptibility and θ_L can be taken from the B-phase as well. Still the $\hat{\mathbf{n}}$-vector has a preferred orientation, due to magnetic field and surface effects, and a resonance frequency shift, as described in equation (3.9), can indeed been seen in the figure.

Section 3.4 explained that for a cylindrical symmetric container with an axial magnetic field, in which the radius is at least a few times the magnetic healing length ξ_B, a flare-out texture can be expected. For temperatures near T_c the healing length is indeed smaller than the diameter (1 mm) of the cylinder. However, as explained in the previous section, the healing length increases to approximately 2.5 mm at 0.7 T_c for 6 bar, which is 5 times the radius of the cylinder. One should expect, from energetic arguments, a uniform texture where all the $\hat{\mathbf{n}}$-vectors have an angle β (angle between the $\hat{\mathbf{n}}$-vector and external applied magnetic field $\mathbf{B}_0$) of $\cos^{-1}(1/\sqrt{5})$.

The line shapes in figure 3.7 show that such a uniform texture is not created. As the temperature decreases [6] the absorption spectrum becomes wider, meaning that the orientation of the $\hat{\mathbf{n}}$-vector radially changes in the cylinder. A more peculiar phenomenon becomes clear for temperatures below 0.7 T_c. One can notice spin waves in the NMR spectrum. The spin waves are more or less equally separated, but more importantly they have approximately the same intensities. This effect, as described in section 3.5.1, is expected for textures in a flare-out configuration, which forms a quadratic potential. For the lowest temperatures (at 6 bar) one can clearly distinguish 5 spin wave modes, lower pressures reduce the amount of modes. This pressure dependence will be worked out in detail in the following section.

---

[5] In an ideal adiabatical magnetization system the ratio between magnetic field and temperature is constant, $B/T = B^*/T^*$. If one starts with a magnetic field B^* the current magnetic field can be expressed as $B = B^* + \Delta B(t)$, where $\Delta B(t)$ is the increased amount of magnetic field after $t = 0$.

[6] Technically the data is obtained with increasing temperature, but has the same behavior for decreasing temperatures. See remark next paragraph.

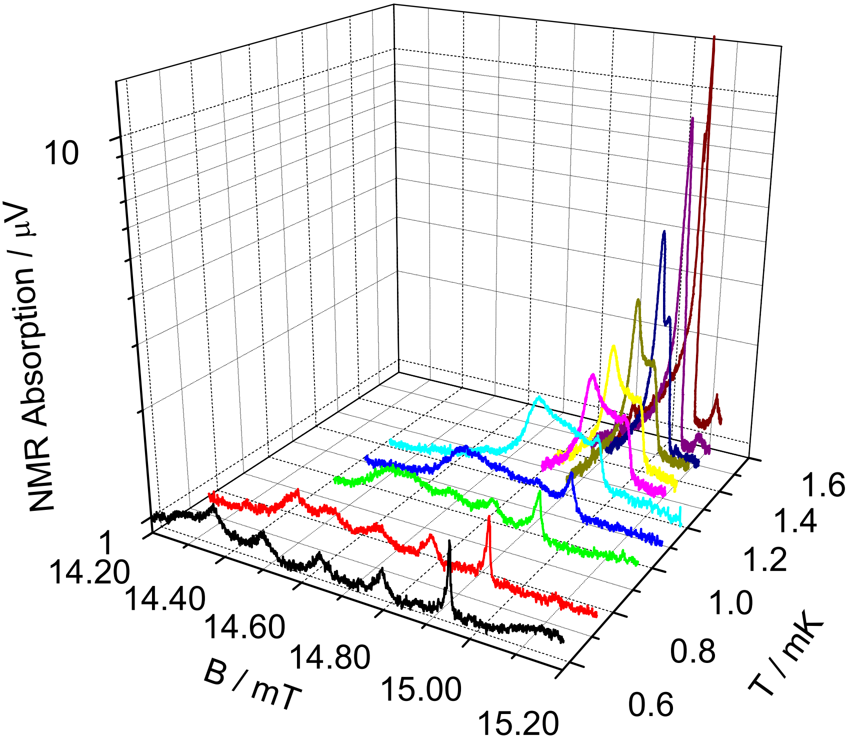

Figure 3.7: NMR absorption scans of helium in a cylinder with a radius of 0.5 mm at 6 bar for various temperatures. The absorption is expressed in μV, which is the signal measured with the pick-up coil. The temperature range is between 0.57 mK and T_c (1.56 mK). At the transition temperature the absorption peak is in resonance at the Larmor frequency, lower temperatures show a shift of the resonance frequency due to texture effects. At even lower temperatures, $T/T_c < 0.7$, several spin waves modes become visible.

At this point it should be emphasized that the cell was always pressurized in the normal phase. So, before the start of every measurement, the liquid was cooled from the normal phase to the superfluid phase. The data presented in this thesis are obtained at increasing temperature sweeps, which gives quantitatively better temperature reliability, however decreasing temperature sweeps show qualitatively the same results. Beginning the cool down above T_c starts the texture in the flare-out configuration. Increasing the magnetic healing length [7] does not show any textural transition. Somehow the texture seems to get stuck in this configuration.

3.8 Metastable texture

From the data shown in figure 3.7 one can conclude that the $\hat{\mathbf{n}}$-vector finds itself still in the flare-out configuration. Somehow it does not make a transition to another textural distribution. It may be that such a transition corresponds with sharp jumps of the $\hat{\mathbf{n}}$-vector, which will definitely be discouraged by the bulk-bending free energy. If that is the case, one can consider the flare-out configuration, at low temperatures, as a metastable state.

Assuming the state is still in the flare out configuration for such long magnetic healing lengths, it is unclear how the angle β radially distributes over the cylinder, except that the boundary conditions determine that β should increase from 0 at the center to $\cos^{-1}(1/\sqrt{5}) \approx 63.4^\circ$ degrees at the surface. From figure 3.5 one can see that for increasing magnetic healing lengths the curve becomes straighter. Here simulations for magnetic healing lengths up to half of the radius were presented, which could still be performed in a linear regime. Longer magnetic healing lengths make these calculations hard or unreliable. However, by extrapolating the curves, one can assume that in the most extreme case of a flare-out configuration β will increase proportionally with r. In other words, the $\hat{\mathbf{n}}$-vector changes gradually from the surface to the center, which is also the distribution giving the lowest bending free energy.

The potential of equation (3.27), assuming that $\beta(r)$ is proportional with r, is plotted together with a quadratic potential in figure 3.8. The maximal relative difference between those two potentials is 6.5%. To analyze our data we do not consider this difference problematic, so that we can replace the potential in the differential equation (3.28) by a quadratic potential, to get an analytically solution. By combining the equations (3.26), (3.29) and (3.6) we get:

$$(\omega_k - \omega_L)\omega_k = \frac{6\gamma^2}{\chi_B} g_D(T) \sqrt{\left(\bar{K} - \frac{1}{2}\bar{K'}\right)} \frac{\xi_D}{L_1}(k+1). \tag{3.32}$$

In literature [83], [62], [79] one of the most important temperature dependency concerning the spin waves modes is the growing (or decreasing) magnetic healing length. As in our case the texture appears to be 'stuck', the effective magnetic healing length seems to stay constant for temperatures of $T/T_c < 0.7$, and so should L_1. In this quadratic potential and cylindrical cell with a radius of 0.5 mm the length $L_1 = \sqrt{5/2}\, R \approx 7.9 \cdot 10^{-4}$ m.

The dominating temperature dependencies are coming from the gap energy $\Delta(T)$ and the spin susceptibility $\chi_B(T)$. By combining the equations (1.3), (1.4), (1.5), (1.6), (1.21), (1.32), (1.33), (1.36), (3.6) and using the definitions of $\bar{K}$ and $\bar{K'}$ from

---

[7] It is increasing by decreasing the temperature.

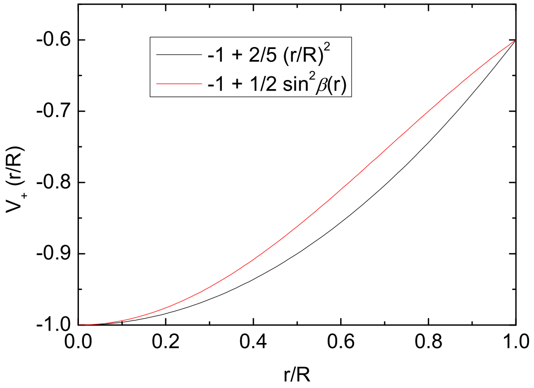

Figure 3.8: The potential V_+ and a quadratic potential in a cylindrical symmetric container of radius R are plotted as function of r. Here it is assumed that $\beta(r)$ is proportional with r. The only requirement for the quadratic potential is that it has the same boundary conditions as V_+, meaning it varies from -1 in the center to $-3/5$ at the surface.

(3.20) we can rewrite (3.32) as

$$(\omega_k - \omega_L)\omega_k \approx 6\sqrt{\frac{14\zeta(3)}{240\pi^3}}(1.76)^2\gamma(1+F_0^a)\sqrt{\frac{{v_F}^3}{\hbar^3}}k_B T_c \frac{m^*}{L_1}\times \ln\left(\frac{2\varepsilon_c}{1.76 k_B T_c}\right)\frac{\chi_N}{\chi_B(T)}\frac{\Delta(T)^2}{\Delta(0)^2}(k+1). \tag{3.33}$$

The equation is now expressed in natural constants and pressure dependent observables as listed in the appendix A.1. The temperature dependence of $\Delta(T)/\Delta(0)$ and $\chi_B(T)/\chi_N$ are plotted and fitted in appendices A.2 and A.3, respectively.

The following two graphs (figures 3.9 and 3.10) contain the (average) position of the spin wave modes, as function of temperature, for 0 and 6 bar, respectively. Also the theoretically expected positions, according to equation (3.33), are plotted. The position is expressed as their frequency multiplied with the difference between the Larmor frequency. Data of the spin waves peaks are from temperatures below $T < 0.7T_c$, for which the overlap of the peaks is reduced enough, so they can be distinguished from each other.

The separations of the peaks are not perfectly equal. However, at higher pressures this seems to improve, which probably means that the potential is better approximated by a quadratic one. The maximal relative difference between the data and theory is over 20 %, however the essence of measurements can be explained by theory. More important the number of modes seems to grow as function of pressure. For zero

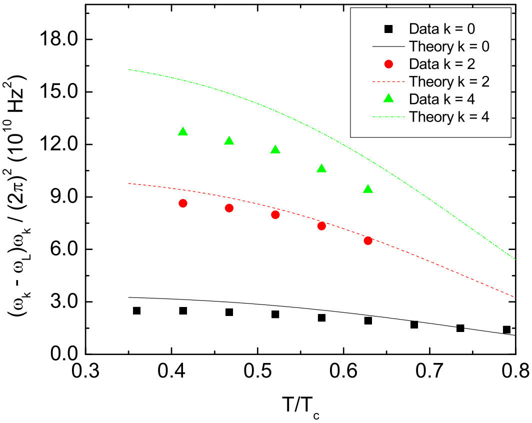

Figure 3.9: Here the spin wave data, at 0 bar, are plotted as function of reduced temperature. The data points correspond to the positions of the spin wave modes as observed in the measurement. The lines correspond to the positions of the peaks as predicted by theory. In total 3 modes are detected.

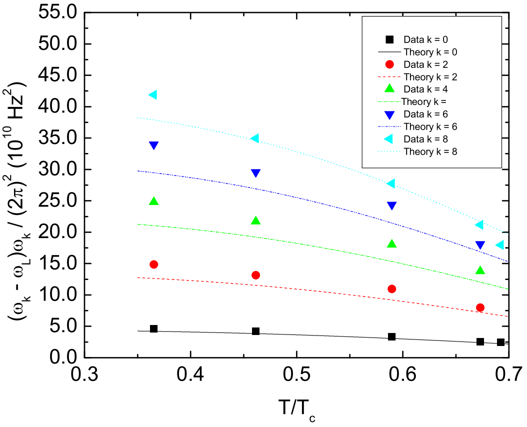

Figure 3.10: Here the spin wave data, at 6 bar, are plotted as function of reduced temperature. The data points correspond to the positions of the spin wave modes as observed in the measurement. The lines correspond to the positions of the peaks as predicted by theory. In total 5 modes are detected.

pressure 3 modes are observed, to 5 modes for 6 bar.

The geometrical pre-factors and L_1 [8] are constant. The dipole coherence length ξ_D, see equation (1.37), is proportional to the coherence length ξ_0, which depends on pressure. We use equation (3.29) to calculate the amount of spin waves that can be formed in this potential. In the weak-coupling Ginzburg-Landau limit the eigenvalues are only pressure dependent. Than $\bar{K}$ and $\bar{K}'$ are 8/5 and 4/5, respectively. In this limit only the dipole coherence length ξ_D change as function of pressure, which can be tuned between 32 (zero pressure) and 7 μm (melting pressure). The energy difference between the modes of equation (3.29) is decreasing as function of pressure and as the potential (at least for $T/T_c < 0.7$) is unchanged more spin waves can exist in the system by higher pressures. Of course only discreet numbers of modes can exist.

The spin wave modes for several different pressures obtained at the lowest achievable temperatures are shown in figure 3.11 and their relative intensities in figure 3.12. The theoretically predicted positions of the spin wave peaks at zero temperature [9] are plotted as well.

The measurements are in good qualitative agreement with the theory. Still the trend is that the theory predicts smaller spacing between the frequencies of the spin modes. Higher spin wave frequencies (bigger spacing) are expected for steeper increasing potentials, and as shown in figure 3.8, V_+ is indeed steeper than the quadratic potential (except close to the cell wall). This may explain the mismatching between the two. Also the amount of spin modes is as predicted by theory. There is one exception, for zero pressure one would expect 2 spin wave modes, however we see 3 modes. The frequency of the highest mode, see green line in figure 3.9, has the largest differences from the theory and its intensity, which is different from the normal trend, as we will show later. Somehow it seems to be a half mode, a spin wave which is seen to be into the system. Another possibility is that it is a side effect due to the finite length in the z-direction. Nevertheless, the reason is not very clear and the effect is only visible for zero pressure. At higher pressures (above 1 bar) such artifacts do not appear and seem to be in (reasonable) agreement with theory.

The width of the absorption peaks gets wider for higher k and increases maximally by a factor of 5. We believe that the most important cause of this is due roughness at the wall. The cell is made of the plastic Polyetherimide PEI of which the surface is relatively rough. As the transverse component is maximal at R (at the wall) one would expect to see the most surface effects for higher k, for which the weight of the wave function is closer to the surface. More peculiar is that the intensity of each mode is increasing as function of k, as is shown in figure 3.12. Here the relative intensity can increase to 2.5 - 3 times. For a $2D$ harmonic oscillator in a cylindrical symmetry one would expect the same intensity for all k-modes (solid lines of figure 3.12), a consequence of the behavior of the density of states in this $2D$ system (with quadratic potential), which is then a constant. An increase of the intensity for the higher k-

---

[8] As we have assumed.

[9] The obtained data is from temperatures lower than 0.3 T_c. As can be seen from appendices A.2 and A.3 only very small changes due to temperature are expected, which makes to data suitable to compare with zero temperature theory.

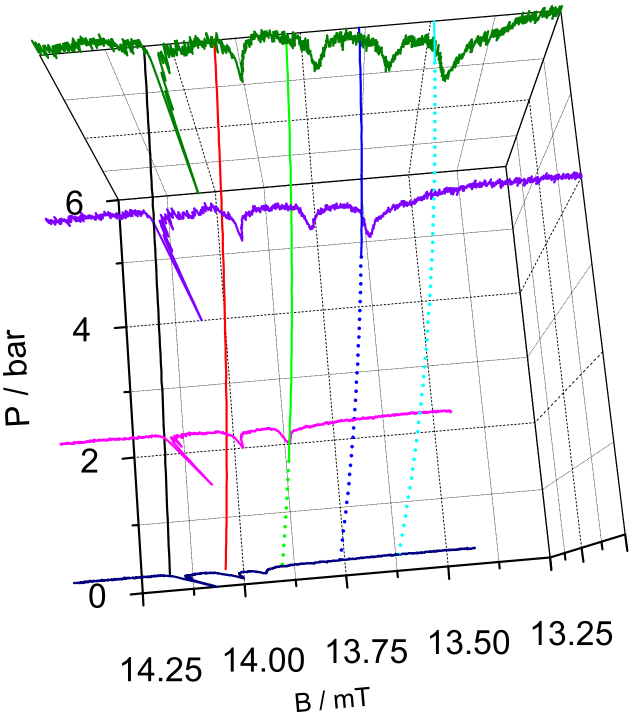

Figure 3.11: Spin wave absorptions peaks as function of magnetic field by pressures of 0, 1.5, 4 and 6 bar. The absorption is expressed in arbitrary units and corresponds with temperatures below 0.3 T_c. The longest peak corresponds with mode $k = 0$, the neighboring peak to the mode $k = 2$, and so on. The curves are the theoretically predicted spin wave frequencies at zero temperature. Black, red, green, blue and cyan correspond with the mode 0, 2, 4, 6 and 8, respectively. All curves are plotted (dotted) for increasing pressures (started from 0 pressure), but become solid when theory predicts the mode to exist.

modes is what one would expect if the potential would increase faster compared to a quadratic potential (and a constant density of states).

By taking the density of states constant, the potential energy is known at the boundary (surface) and using the relative increase of the intensities as given in figure 3.12, we could reconstruct the potential, as plotted in figure 3.13, in our cell as it should be according to our data. The reconstruction of the potential was done for all four pressures. However, we believe that data for the higher pressure is more reliable,

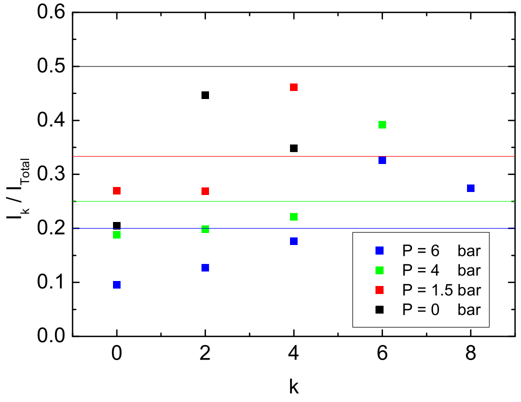

Figure 3.12: The relative intensities of the k modes from the data of figure 3.11. The scattered data are the estimations of the measurements, well the lines correspond to the theoretical prediction if the potential is perfectly quadratic. Black, red, green and blue squares corresponds to the pressures of 0, 1.5, 4 and 6 bar, respectively.

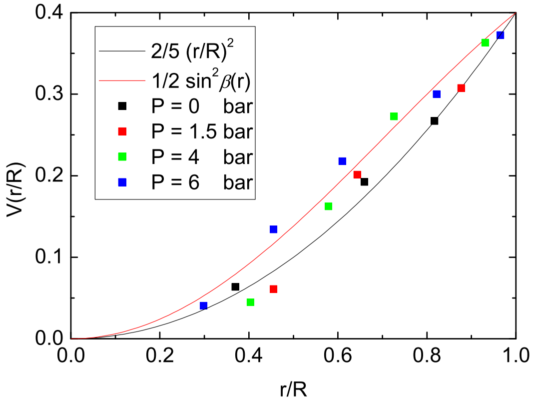

Figure 3.13: The reconstructed potential from the data of figure 3.12. The data points are calculated values of the potential as function of the radius for different pressures. Black, red, green and blue squares correspond to the pressures of 0, 1.5, 4 and 6 bar, respectively. The solid lines are the potentials discussed in figure 3.8.

since the reconstructed data points of the potential coincide with the amount of spin waves modes. If one can compare more absorption peaks with each other, the errors will reduce. Also the spatial dependencies become clearer with more data points.

The potential (especially clear for the higher pressures) seems to follow the potential of $1/2 \sin^2 \beta(r)$ for $r > 0.5R$, for small r there seems a trend to drop faster. However, the lack of sufficient data makes it hard to give a strong statement. To investigate the potential at small r, measurements at higher pressures should be performed. Presently we can conclude that our results are consistent with a proportionality of β with r for $r > R/2$.

3.9 Textural transition

The textural configuration described in the previous section is from energetic point of view not the expected state. However, it seems to be a stable state and once the superfluid is in this configuration no transition to another textural configuration is observed. Most cool downs were executed with a relatively slow speed rate, to be sure that the nuclear stage was cooled adiabatically. Faster [10] cool downs would sometimes show, at least initially, a more uniform shift of the absorption peak. This phenomenon made us realize that the creation of a flare-out texture is correlated with a sufficiently slow enough cool down. As already mentioned in the previous section, the slowly growing texture is forced to stay in this configuration, as the threshold to jump to a different may be too high.

If one would cool down more rapidly, the magnetic healing length ξ_H^B would grow and oversize the radial dimension of the system much faster than in normal procedure. At the moment the superfluid is formed the $\hat{\mathbf{n}}$-vector is not given the time to grow smoothly into the flare-out configuration. The surface will dominate the forming of the configuration, and a completely uniform texture would be expected. One of the fastest ways to cool down the liquid would be to cool the system to lowest temperatures, and then locally (while the rest of the system is kept cold) warm the superfluid above T_c. At the moment the liquid is in the normal state one should stop the heat input, so that the locally heated liquid will cool down to the initial temperature. The heat only needs to be removed locally, instead from the whole system, which makes the cooling of the liquid considerably faster.

By doing NMR, one always heats the sample locally. As explained in section 2.4 the absorption signal actually shows the change in the fractional resistance $\Delta R/R_0$. The ΔR is the dissipation due to NMR and the average power dissipated in the liquid is then equal with

$$\bar{P} = i^2 \Delta R, \tag{3.34}$$

with i the average alternating current through the coil. As the field lines of $\mathbf{B}_1$ are almost uniform over the whole sample, most dissipation (at least till first order) occurs in the volume between the two coils of the Helmholtz tank coil, see figure 2.15. Increasing the voltage over the tank circuit, would increase the power absorbed into the liquid in this volume. The energy needed to make the superfluid (at $T = 0$ K)

---

[10] The speed rate of the cool down should still be in the adiabatically regime, but faster than the usually procedure.

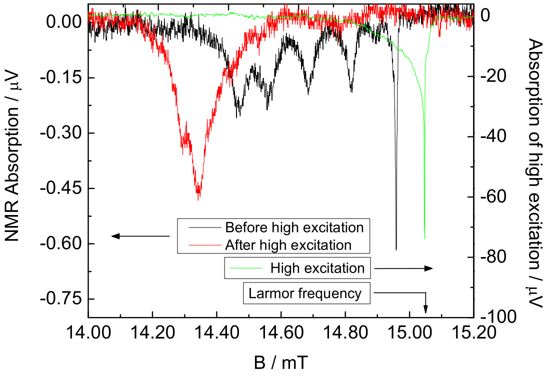

Figure 3.14: Local heating of the superfluid with NMR. The black and red curves show the absorption spectrum of 6 bar at 300 μK before and after heating the sample, respectively. The corresponding values of both absorption curves are put on the left y-axis. The green curve corresponds with the absorption curve while heating the sample, absorption values are put on the right y-axis. Here the values are 2 orders of magnitude higher, so enough energy is dissipated to locally warm up the liquid to the normal state, as is indicated by a jump of the peak to the Larmor frequency. After the local heating, the texture is changed from flare-out to a uniform configuration.

normal, is roughly equal the product of the volume and the energy density of equation (1.9). For 6 bar this is approximately equal to

$$(F_n - F_s)\ V \approx \frac{1}{4} N_F (1.76\ k_B\ T_c)^2\ V \approx 2.58 \cdot 10^{-9}\ \text{J}. \tag{3.35}$$

To overcome this energy threshold one should dissipate sufficiently long, since the power is low. However, ^{3}He in the superfluid state is a good thermal conductor and to be sure that the liquid is only heated locally, one should pump the energy relatively fast into the system. In principle one could calculate how much voltage should be put over the tank circuit to dissipate enough power, but it is a complicated problem since the increasing voltage changes the parameters like the Q [11] of the tank circuit. In practice one can easily notice when enough energy is dissipated, as one can see that the frequency of the absorption peak(s) shift back to the Larmor frequency.

Let us start from the situation at 6 bar (around 300 μK) with the usual spin waves, which correspond to the black curve in figure 3.14. From here the excitation is inflated

---

[11] Higher voltage increases the current in the tank circuit. More current give more dissipation, and a new situation where heat in- and output are in equilibrium need to be established. For the usual excitations, the current is small enough that it is not the dominating dissipation factor, and no effects on the Q can be seen.

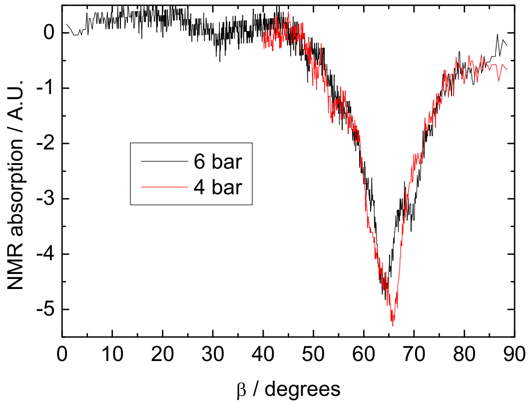

Figure 3.15: Absorption spectrum convert to β dependency. Here the data for 4 and 6 bar (at 300 μK) are presented. The data show a Lorentzian behavior, for where the center is around 64.7°. FWHM is around 10.5° and is considered mainly due to surface roughness.

to ~ 6.4 mV, which is 100 times more than in the usual NMR experiments. The result is the green curve, from which one can estimate ΔR ($4.57 \cdot 10^{-4}$ Ω). As described in section 2.4, one can calculate the current i through the coil ($2.24 \cdot 10^{-4}$ A). The average power dissipated is then $\bar{P} = 2.29 \cdot 10^{-11}$ W. The sweep through resonance takes about a minute, so the total amount of dissipated energy is $\sim 1.37 \cdot 10^{-9}$ J. If one compares this with the upper limit (3.35), it is certain that the amount of heat dissipated in the superfluid is enough to put it in the normal state. This is corroborated by the fact that the absorption peak jumps to the Larmor frequency, where the width is mostly determined by the inhomogeneity of the magnet.

To limit the total amount of heat input, the voltage is immediately reduced to its initial value if the jump to the Larmor frequency is observed. The local heated liquid starts to cool and the absorption peak moves uniformly to the left as the liquid becomes superfluid. The red curve in figure 3.14 shows the equilibrium result, when the liquid is cooled back to 300 μK. The spin wave modes have disappeared, and the NMR absorption signal only shows a single peak, indicating that the superfluid is in a uniform texture. The total absorption (intensity) of both line shapes are equal, which is expected as the total amount of atoms is equal.

This procedure is repeated for several different pressures and all show the same behavior. Using equation (3.9), which gives the relation between the signal frequency and the angle β of the $\hat{\mathbf{n}}$-vector with respect to $\mathbf{B}_0$, we can plot the absorption spectrum as function of β. This is done for 4 and 6 bar in figure 3.15.

The curves show a Lorentzian behavior, whose center is around 64.7° with a

FWHM of 10.5°. The angle is sufficient close to the expected 63.4°. The deviation is most likely dominated by the imperfect alignment between cylinder axis and magnetic field. It seems reasonable that 1.5° difference, compared to perfect parallel alignment, is noticeable. So, we indeed see a uniform texture with the angle as expected from energetically arguments. The width of the peak is wide compared to the absorption peaks from the spin waves. As now the direction of the texture is completely determined by the cell wall, one would expect a full reflection of the roughness in the NMR spectrum. It is understandable that roughness broadens out the NMR signal, but it is hard to make a quantitative conclusion from the width, as different wall roughness can give the same width.

Once this new texture is created it seems to be a stable state as well, even if the superfluid is warmed up (of course one stays under the T_c of the superfluid), no transition is noticeable. However, we do see a change as the helium bath of the cryostat is refilled. The filling line (capillary) of the cell goes through the bath and there was no possibility to close this capillary near the cell. The pressure in the capillary is thus the pressure which pressurizes [12] the cell. At the moment we start filling the helium bath, (relative) warm gas flows over the capillary and later when the refilling continues liquid ^{4}He surrounds it. In other words the equilibrium situation is disturbed. At each liquid helium transfer, the fluctuation in the pressure gets enough that the liquid is warmed up to the normal phase. The moment the fluctuations are small enough that the system can be cooled again [13], it grows into the flare-out texture.

The nuclear stage may warm up by vibrations [14] created due to filling. It is considered to be a small effect, even in this case the temperature of the environment is already cold. However, the fact that the liquid as a whole had to be cooled again seems to be sufficient to let the texture grown into the flare-out configuration. We did not study systematically the influence of the cooling rate on the type of texture, as that was too difficult concerning the configuration of our cryostat.

3.10 Discussion

From what we have encountered in our experiments, we were able to create a stable flare-out texture till the lowest temperatures. From the energetically point of view it was a surprising effect, and as pointed out by the experiments of local heating, the cooling rate played an important role of the forming of the texture. The configuration of our experimental cell made it too difficult to do better quantitatively cool down experiments. Better cooling experiments should be achieved in cells such as the

---

[12] The pressures used in the experiments are such that no plug (solid) is formed in the capillary as in contrast with the melting curve thermometer.

[13] Our experience is that the warm gas through the transfer tube is responsible for the increase of the fluctuations. Once the transfer tube is cooled enough, so liquid ^{4}He is transferred, the fluctuations are reduced enough that the liquid in the cell cools again.

[14] Most dissipation induced by vibrations arises when the magnet and nuclear stage move with respect to each other, which creates eddy current heating.

Pomeranchuk cell.

It seems that the texture, where the order parameter is given enough time to grow into the flare-out configuration stretched over the sample, is incredibly stable. Using the knowledge we have of the magnetic healing length ξ_H, it is clear that other textural configurations must cost less energy. However, to go to this 'new' configuration there should be a transition between the two textures. A spontaneous transition to the uniform texture (as founded by local heating) will coincide with sharp jumps of the $\hat{\mathbf{n}}$-vector, such transition which will definitely not be appreciated by the bulk-bending free energy, maybe a possible reason why the texture will stay in the flare-out configuration. The dynamics of transitions is in general hard, and in the case of static experiments not much is reported in literature.

The stable flare-out texture gives us a good opportunity to study spin waves over the whole temperature regime. The cylindrical geometry in combination with a diameter of 1 mm gives us a constant (transverse component) potential below temperatures of 0.7 T_c. This constant potential [15] made it possible to observe how spin waves grow in our sample. Also the relative intensities of the spin waves did not decrease for the higher spin modes, this in contrast with the reported spin waves in similar configurations. This effect is maybe desirable in experiments concerning the dynamics of vortices in such a cylinder, since now the higher modes have too bad signal to noise ratio and no information can be retracted of them.

The spin waves let themselves describe in good agreement as is derived from the spin dynamics in cylindrical symmetry. While we compare the data presuming we had a quadratic potential, which gave the advantage that the model was analytically solvable, we could reconstruct to a large extent the actual potential by comparing the data and theory. Naturally the two potentials did not differ too much, but we could note that (at least for big r) β is proportional with r. This would correspond with a gradually change of the $\hat{\mathbf{n}}$-vector between the two boundary conditions, a scenario which seems imaginable as an extreme flare-out configuration.

The local heating experiment showed that it was possible to create the uniform texture in our cell, and not unimportant showed to have an average angle close to 63.4°. Good confirmation that the surface-field free energy has strong influence on this texture, and that it is in agreement with theory. This technique may be used to create two different textures close to each other, for which the dynamics or transition between them can be studied.

3.11 Conclusion

In conclusion, with the carefully chosen geometry in combination with low pressures and low magnetic fields, we could make a metastable $\hat{\mathbf{n}}$-texture. The texture was

---

[15] Most spin wave experiments are done in cylinders with a diameter of few times ours, and often performed at higher pressures. Consequently the ratio between radius and magnetic healing length ξ_H is bigger than in our case, and thus the shape of the potential changes with decreasing temperature. In the analysis of those spin waves the change of ξ_H was considered the most important temperature effect, a temperature dependence we could exclude from our analysis.

stable and unchanged for a significant part in the pressure and temperature ranges. It functions as a potential to create spin waves, which made it now possible for us to study them for several pressures in exactly the same texture (potential). As this potential (texture) is close to a quadratic one, and this is essentially a two dimensional system, the intensities of all spin wave modes are nearly equal. This is an excellent system to observe the grow of spin waves modes in our cell by increasing the pressure. The theory, which we adapted for our geometries and boundary conditions, could very well describe the found results, making our physical understanding of this phenomenon complete.

Finally we were able to make a textural transition to the in advance expected texture, for which we conclude that the metastable texture could be realized if the growing speed is sufficiently slow.